Scanning tunneling microscopy observation of the hinge states of bismuth nanocrystals

Tianzhen Zhang,[1,2] Sergio Vlaic,[2] Stéphane Pons ®,[2] Dimitri Roditchev,[2] Valeria Sheina,[3] Christophe David,[3] Guillemin Rodary,[3] Jean-Christophe Girard ®,[3] and Hervé Aubin[2,3,*]

[1]*Interdisciplinary Materials Research Center, School of Materials Science and Engineering, Tongji University, Shanghai 201804, Peoples Republic of China*

[2]*Laboratoire de Physique et d'Étude des Matériaux (LPEM), ESPCI Paris, PSL Research University, CNRS UMR8213, Sorbonne Université, 75005 Paris, France*

[3]*Universités Paris-Saclay, CNRS, Centre de Nanosciences et de Nanotechnologies (C2N), 91120 Palaiseau, France*

The recent application of topological quantum chemistry to rhombohedral bismuth established the nontrivial band structure of this material. This is a second-order topological insulator characterized by the presence of topology-imposed hinge states. The spatial distribution of hinge states and the possible presence of additional symmetry-protected surface states is expected to depend on the crystal shape and symmetries. To explore this issue, we have grown bismuth nanocrystals in the tens of nanometers on the (110) surface of InAs. By scanning tunneling spectroscopy, we mapped the local density of states on all facets and identified the presence of the hinge states at the intersection of all facets. Our paper confirms the classification of bulk bismuth as a second-order topological insulator. We propose that the ubiquitous presence of the hinge states result from their tunnel coupling across the nanometer-sized facets.

I. INTRODUCTION

Solids with filled electronic bands and no interactions may seem quite mundane, yet, band structures can have interesting nontrivial topological properties that can be inferred from their symmetries.

To analyze the symmetry properties of an atom located on a lattice site, it is usual to employ the representation theory [1] of point groups to obtain the decomposition of the atomic orbitals as a direct sum of irreducible representations of the atomic site point-group symmetry.

By analogy, to analyze the symmetry properties of the Bloch states arising from these orbitals, band representations theory, a representation theory of space groups [2,3], can be employed to obtain the decomposition of the band structure as a direct sum of irreducible band representations.

Although band representation theory was barely used for decades, it have recently attracted intense interest with the demonstration that one band that cannot be decomposed into any linear combination of physical elementary band representation must have nontrivial topological properties. This gave birth to *topological quantum chemistry* [4] and enabled the identification and calculation of symmetry indicators for the 230 space groups [5–7], which are related to topological indices and facilitated large-scale search across databases to identify topological materials [8]. This has greatly expanded the topological classification of band insulators beyond the Z_2 topological insulators [9,10] and revealed the existence of numerous symmetry-indicated topological phases, such as mirror-symmetry-protected topological crystalline insulators

(TCIs) [11,12], rotational-symmetry-protected TCIs [13], and higher-order topological insulators (HOTIs) [14–18].

Although the lowest-symmetry HOTI models exhibit gapped two-dimensional surface states and gapless one-dimensional hinge-states [5–7,18], typical solid-state HOTIs have additional crystal symmetries that can protect gapless surface-states; thus, a HOTI can coexist with a TCI. Depending on the sample termination, the same crystal may exhibit either two-dimensional surface-states or gapped facets separated by topological hinge states.

The application of topological quantum chemistry to rhombohedral bismuth (Bi), with space-group $R\bar{3}m$ (No. 166) and point-group D_{3d} has shown that its valence and conduction bands result from a split elementary band representation [17], which implies nontrivial topological properties. These topological properties result from a double band inversion [11,19] at the same time-reversal-invariant momenta points. The topological phase can be described as two superposed copies of a TCI protected by time-reversal T, threefold rotation $C_{3[111]}$ about the [111] direction and inversion I symmetries [17], characterized by the $Z_4 = 2$ topological index [5–7,15,18]. The fourfold Dirac surface states of this topological phase are unstable [18,20] and it has been shown that a crystal with an inversion-symmetric shape, such as a rod of hexagonal section oriented along the [111] direction, the mass of the Dirac states is of opposite sign on surfaces with inversion-related Miller indices, resulting in helical hinge modes encircling the crystal [17].

Experimentally, on hexagonal cavities in the (111) surface of *bulk* Bi [21], scanning tunneling microscopy (STM) and spectroscopy (STS) identified edge states on every two edges of the cavity. Because two-dimensional bismuth was predicted theoretically to be a two-dimensional quantum spin

Hall insulator (QSHI) with Kane-Mele index $Z_2 = 1$ [22,23], the edge states were identified with the topological states of a QSHI altered by the coupling to the bulk [21]. Although later, STM works indeed confirmed the presence of topological edge states on thin bismuth films [24,25] and bismuthene [26–28], those observed on *bulk* Bi cavities were later reinterpreted as the signature of the hinge states of a HOTI [17]. Interestingly, the edge states in bismuthene and hinge states in Bi are related as it was shown that the stacking of multiple two-dimensional QSHI leads either to a weak three-dimensional topological insulator or a HOTI. $Bi_{14}Rh_3I_9$ [29,30] and Pt_2HgSe_{30} [31–34] are examples of the former; Bi[17], WTe_2[18] and Bi_4Br_4 [35] are examples of the latter. Finally, the presence of the hinge states was also inferred from superconducting quantum interference device like supercurrent oscillations observed with Josephson circuits fabricated on Bi [17,36] and WTe_2 [37–39].

In addition to the HOTI phase protected by the $C_{3[111]}$ symmetry, it has been shown [40] that Bi is also host of a first-order TCI state protected by a twofold rotational symmetry $C_{2[1\bar{1}0]}$ about the $[1\bar{1}0]$ direction, resulting in a pair of topological Dirac surface states on its $(1\bar{1}0)$ surface, coexisting with the hinge states of the HOTI phase. On (110)-oriented Bi films, recent STM/STS measurements [41] have identified hinge states that could be described by a HOTI protected by time-reversal symmetry and bulk twofold rotation $C_{2[1\bar{1}0]}$ [40]. The surface states were not observed though because of the broken translation symmetry on the $(1\bar{1}0)$ facets.

These recent theoretical and experimental works suggest that the distribution of surface and hinge states on a Bi crystal depends on its shape and transformation properties under $C_{3[111]}$, $C_{2[1\bar{1}0]}$ and inversion symmetries.

To explore the relationship among surface states, hinge states, and the crystal shape, we have grown Bi nanocrystals on the (110) surface of InAs and characterized its electronic properties by STM/STS. Thanks to the small size of the nanocrystals and using very sharp STM tips, we have been able to perform the STM/STS characterization of multiple facets and hinges of the nanocrystals. We clearly identified hinge states, confirming qualitatively the classification of Bi as a HOTI. However, we found that the spatial distribution of the density of states due to hinge states could not be reproduced easily by a simple model with hinge states appearing at the intersection of facets with Dirac masses of opposite signs [17,40]. Instead we found hinge states at the intersection of all facets, provided they are sufficiently extended. We suggest that the ubiquitous presence of hinge states is the consequence of their hybridization due to tunnel coupling across the nanometer-sized facets.

II. NANOCRYSTAL GROWTH

The Bi nanocrystals have been grown on the (110) surface of n-doped InAs, which substrate has been cleaved in ultrahigh vacuum at base pressure $P \approx 10^{-10}$ mbar. The (110) surface of InAs substrates has also been employed previously for the growth of superconducting Pb nanocrystals [42,43] and Bi nanolines [44,45]. By thermal evaporation, we deposited a nominal quantity of three monolayers of Bi at a temperature of 500 K. This is the optimum temperature for the growth of nanolines [45] where we checked their formation by low-energy electron diffraction. A topographic STM image is shown in Fig. 1(a) where Bi nanocrystals are visible as well as nanolines in the zoom inset. Consistently with past works on Bi nanolines [45], there is no indication of alloying with the InAs substrate. To accentuate the facets and edges, a Laplacian filter $\Delta_{xyz}z(x, y)$ is applied to all topographic images. Figure 1(b) show topographic images zoomed on five selected Bi nanocrysals, labeled I–V. The lateral size of nanocrystals is between 10 and 40 nm, the height is between 5 and 15 nm. To obtain such topographic images free from artifacts resulting from the shape of the tip, a tip-shaping procedure has been employed where the tip is approached into contact with the InAs surface, then, a large current of 1 μA is injected, and the tip is slowly retracted. This tip-elongation procedure is repeated until no effects of the shape of the tip is visible on the topography of the nanocrystals. Using the crystallographic software VESTA@ and employing the crystal structure of Bi, we model the shape of all nanocrystals and show the results below the corresponding nanocrystals in Fig. 1(b). From these Wulf constructions, the crystallographic facets (111), (110), and (100) can be clearly identified for each nanocrystal. The (111) facet is the most stable surface of Bi [46] and can be clearly identified as the largest facet with hexagonal shape. This facet is surrounded by the (110) and (100) facets. The (110) facet has C_2 symmetry and its edges make an angle of $\pi/2$, the (100) facet has C_3 symmetry and its edges make an angle of $2\pi/3$. These two angles are indicated on Fig. 1(c) and allow the identification of the facets.

On the hexagonal cavity studied on the (111) surface of bulk Bi [21], two type of edges were identified with edge A (B) corresponding to the edge with the last Bi atom pointing up (down). We use the same notation. As shown by the atomic model in Fig. 1(c), the location of edges A and B can be identified on nanocrystals, which was not possible on the cavity. Edge A (B) is located at the intersection, i.e., hinge, between the (111) and the (100)[(110)] facets.

III. SCANNING TUNNELING SPECTROSCOPY

On these three-dimensional nanocrystals, it is possible to perform STS on multiple facets. We will now detail the results obtained on two selected nanocrystals. The results for nanocrystal I, which has large (111) and (110) facets, are shown in Fig. 2. The results for nanocrystal IV, which has large (111) and (100) facets, are shown in Fig. 3. Additional STS results for the nanocrystals II, III, and V are shown in Fig. 4. For all nanocrystals, a small Coulomb gap about 25 meV is visible at zero bias as highlighted in Fig. 2(c) and Fig. 3(c). As described in the previous work on Pb nanocrystals [42,43], when a nanocrystal is grown atop a two-dimensional electron gas of Fermi wavelength larger than the nanocrystal lateral sizes, a quantum constriction effect occurs, similar to what was observed in quantum-point contacts, reducing the transmission to values smaller than one quantum of conductance. In this situation, the nanocrystal is only weakly coupled to the substrate and so Coulomb blockade occurs. In our system, the Bi nanowires and nanocrystals have expected Fermi wavelengths in the 10–30-nm range [46], comparable to nanocrystals lateral sizes, explaining the observation of
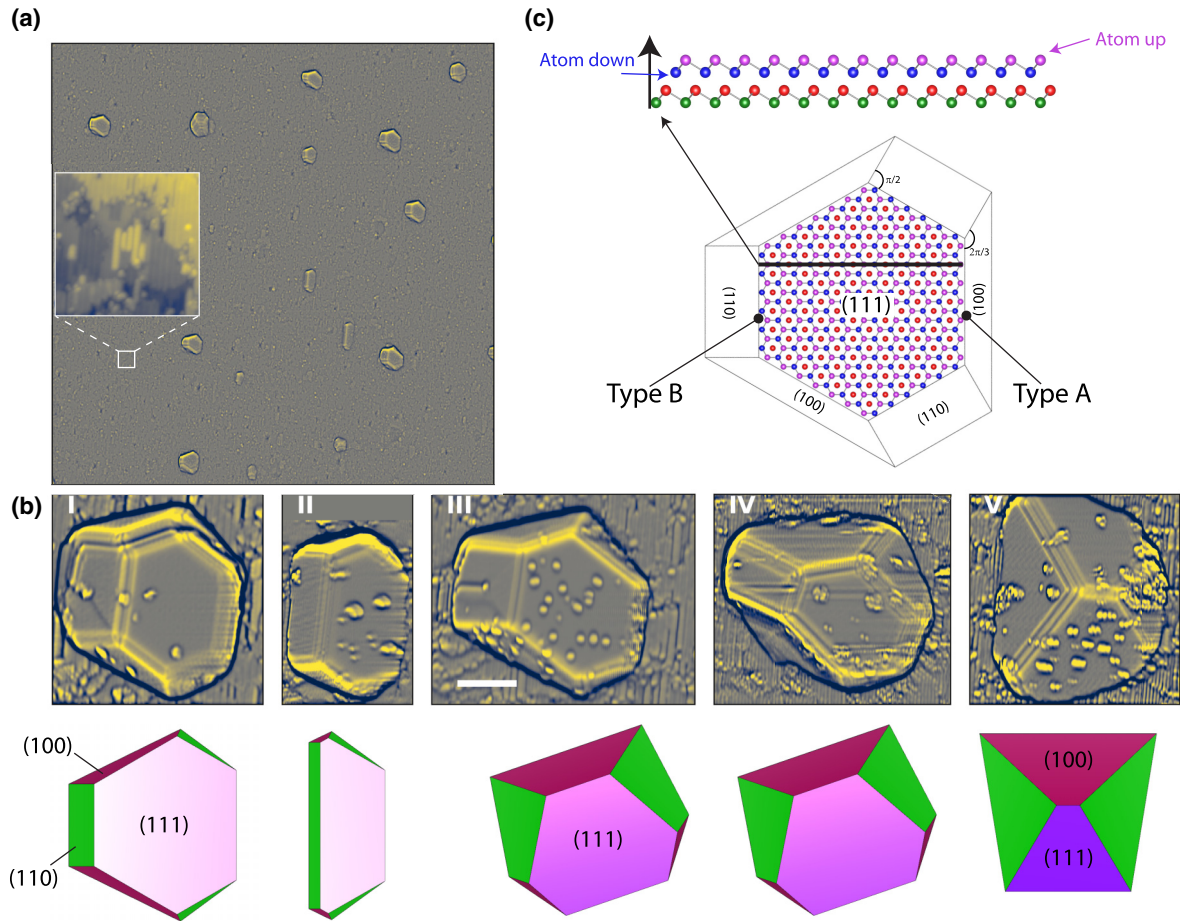
FIG. 1. (a) 800×800 nm^2 Laplacian $\Delta_{xy}z(x, y)$ transform of a topographic STM image ($I_{\text{set}} = 30$ pA, $V_{\text{bias}} = 1.5$ V). The inset is a zoom on a zone 30×30 nm^2. (b) Laplacian $\Delta_{xy}z(x, y)$ transforms of selected topographic images, labeled from I to V. The scale bar on the third image is 10-nm long. Below each image, a model of the shape is provided where are indicated the Miller indices of the facets. (c) Top: Atomic model of two atomic bilayers of Bi. Bottom: Atomic model of a nanocrystal. The type-B edge, last atom of the first bilayer pointing down, is located at the hinge between the (111) and (110) facets. The type-A edge, last atom of the first bilayer pointing up, is located at the hinge between the (111) and (100) facets. As indicated, the edges of the (110) facet make an angle of $\pi/2$, the edges of the (100) facet make an angle of $2\pi/3$.

Coulomb blockade and implying that the Bi nanocrystals are only weakly coupled to the substrate.

Figures 2(c) and 3(c) show the differential conductance (DC) $\frac{dI}{dV}(V)$ spectra measured on nanocrystal I and nanocrystal IV, respectively, at positions indicated by colors symbols on corresponding panels (a) and (b).

In the middle of the (111) facets (red hexagon symbols), the DCs present conductance peaks at $V_{\text{bias}} = 0.23$ V. This is a consequence of the saddle point in the higher-energy relation dispersion of (111) surface states, identified in equations as high-energy surface-states (HESS) [46–48], shown in Fig. 2(g), along the $\bar{\Gamma} - \bar{M}$ direction of the Brillouin zone shown in Fig. 2(e). The corresponding energy range is indicated as green zones in Figs. 2(c), 2(d), 2(g), 2(h), 3(c), and 3(d). The DCs also show a sharp increase near $V_{\text{bias}} = -0.01$ V, which is a consequence of the saddle point in the lower-energy relation dispersion of (111) surface states, followed by a maxima about $V_{\text{bias}} = -0.07$ V, identified in equations as low-energy surfacestates (LESS) where the corresponding energy range is indicated as blue zones in Figs. 2(c), 2(d), 2(g), 2(h) 3(c), and 3(d).

On the edges of the (111) facets, the conductance peak at $V_{\text{bias}} = 0.23$ V due to high-energy surface states is missing, instead, peaks in the DCs are observed at lower energy. For nanocrystal I, conductance peaks are observed at $V_{\text{bias}} = 0.125$ V on all type-B edges (red symbols). On the two type-A edges measured (due to STM drift, the third one has not been measured), one large conductance peak is visible at $V_{\text{bias}} = 0.14$ V on the edge (pink right triangle) where the (100) facet is well defined but only a very small conductance peak ($V_{\text{bias}} = 0.17$ V) is visible on the second one (pink disk); we suggest this is due to the absence of the (100) facet for this edge where the (111) facet is reaching the InAs surface. For nanocrystal IV, on the type-B edges, the conductance peak at $V_{\text{bias}} = 0.125$ V is well defined only on the longest edge (red star symbol) but not on the two other short edges (red left and up triangles). On the type-A edges, the conductance peak at $V_{\text{bias}} = 0.14$ V is visible on two edges (pink right and up triangles), where the (100) facet is well defined, but not on the third one (pink disk symbol) where the (100) facet is absent, and the (111) facet is reaching the InAs surface. As the symmetry arguments employed in topological quantum chemistry
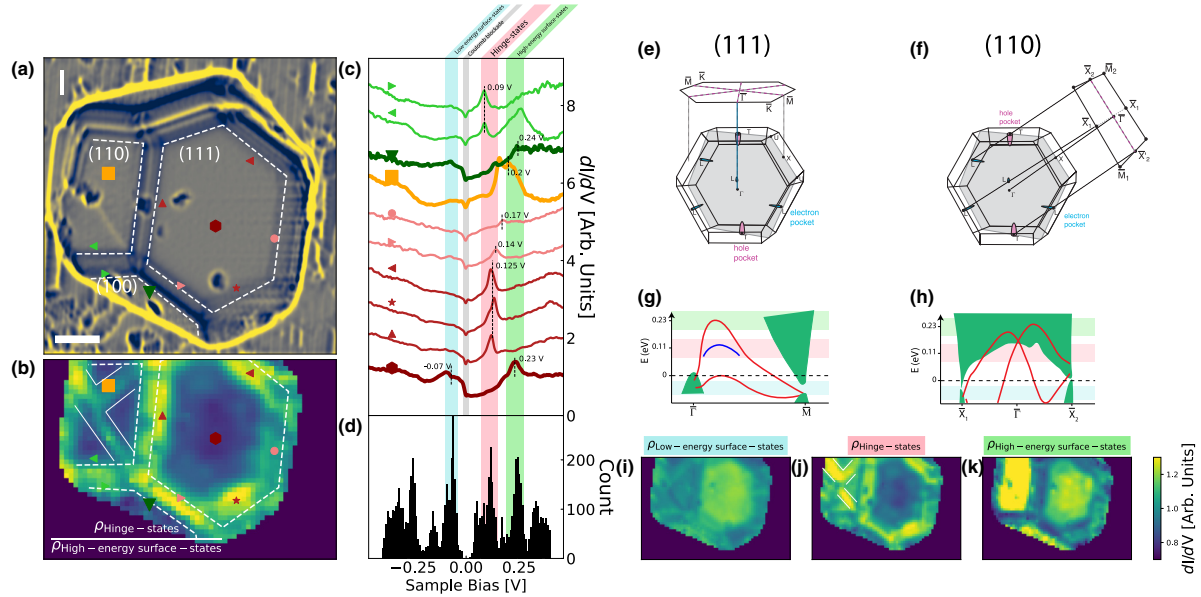
FIG. 2. STS data on nanocrystal I. (a) Laplacian $\Delta_{xy}z(x, y)$ transform of a topographic STM image ($I_{set} = 30$ pA, $V_{bias} = 1.5$ V). The scale bar is 5 -m long. The dashed lines indicate the edges between facets. (b) Conductance map $\frac{\rho_{HS}}{\rho_{HESS}}$ obtained by taking the ratio of the DC integrated on energy range of hinge states ρ_{HS} with the DC integrated on the energy range of high-energy surface-states ρ_{HESS}. The scale is the same as in panel (a). The dashed lines indicate the edges between facets. The white continuous lines indicate the diagonal states generated by the defect in the middle of the (110) facet. Note how they merge with the hinge states. (c) DC for selected points indicated as colored symbols on panels (a) and (b). The vertical colored rectangles indicate the energy ranges of interest corresponding, respectively, to low-energy surface states, Coulomb gap, hinge states, and high-energy surface states. The vertical dashed lines indicate conductance peaks of interest. See the text. (d) Histogram of the energy values of conductance peaks identified in all DC curves measured on the nanocrystal. (e) Bulk Brillouin zone and pseudo-Brillouin zone of the (111) facet. (f) Bulk Brillouin zone and pseudo-Brillouin zone of the (110) facet. (g) Extracted from Ref. [46], the relations dispersions of projected bulk states (green areas), surface states (red lines), and hinge states (blue line) on the (111) facet. (h) Extracted from Ref. [46], the relations dispersions of projected bulk states (green areas) and surface states (red lines) on the (110) facet. (i)–(k) Conductance maps ρ_{LESS}, ρ_{HS}, and ρ_{HESS} obtained by integrating the DCs on energy range of low-energy surface states, hinge states, and high-energy surface states, respectively.

are very strong and do not depend on any particular model or adjustable parameters, the identification of these conductance peaks on both types of edges with the one-dimensional van Hove singularities of the hinge states expected for a second-order topological insulator is one most reasonable assumption.

The hinge states are labeled as HS in equations. Their energy range is indicated as pink zones in Figs. 2(c), 2(d), 2(g), 2(h), 3(c), and 3(d). Thus, in contrast to the observation on cavities in the (111) surface of bulk Bi crystal [21], we find that the conductance peaks due to hinge states are visible on both type of edges. As is also seen on the other nanocrystals, Fig. 4, the conductance peaks are visible only when the two facets making the hinge are extended and well defined.

In the middle of the (110) facet (orange square symbols), the DCs feature broad maxima at $V_{bias} = 0.18$ V, consistent with the observation of Ref. [41]. This maxima in the density of states is due to (110) surface states [46,49,50], whose dispersion relation is shown Fig. 2(h) along the $\bar{X}_1 - \bar{\Gamma} - \bar{X}_2$ direction of the Brillouin zone shown in Fig. 2(f).

In the middle of the (100) facets (green down-triangle symbols), mostly visible in Fig. 3(c) of nanocrystal IV, the DCs feature broad maxima at $V_{bias} = 0.24$ V, which is likely due to (111) surface states [46].

Finally, on the hinges between the (110) and (100) facets (light green symbols), the DCs feature conductance peaks at

$V_{bias} \approx 0.1$ V that indicates the presence of hinge states. This is remarkable as they do not involve the (111) facet, which confirms the classification of Bi as a HOTI.

Two comments are in order.

First, we note that the energy of the van Hove singularities slightly changes from one hinge to the other; in particular, they have energies ≈ 0.125 eV for type-*B* edges and ≈ 0.14 eV for type-*A* edges. This change in energy could be explained by the hybridization between hinge states located on opposite edges of the nanocrystal or because of different relation dispersions for the hinge states on edges with different atomic terminations or arrangements.

Second, on all edges, the van Hove conductance peaks due to hinge states appear concomitantly with the disappearance of the conductance peaks due to surface states on all three facets. Such an anticorrelation was also observed previously [21].

To see this more clearly, we acquired full conductance maps, typically on a spatial grid of 64×64 pixels^2 and 512 voltage points. Figure 2(d) shows a histogram of the energies of the conductance peaks identified in the 4096 DC spectra measured on nanocrystal I. This histogram shows that the low-energy surface states, high-energy surface states, and hinge states are at the origin of all conductance peaks observed in the energy range of [−0.25 to 0.25 eV]. There is no other major
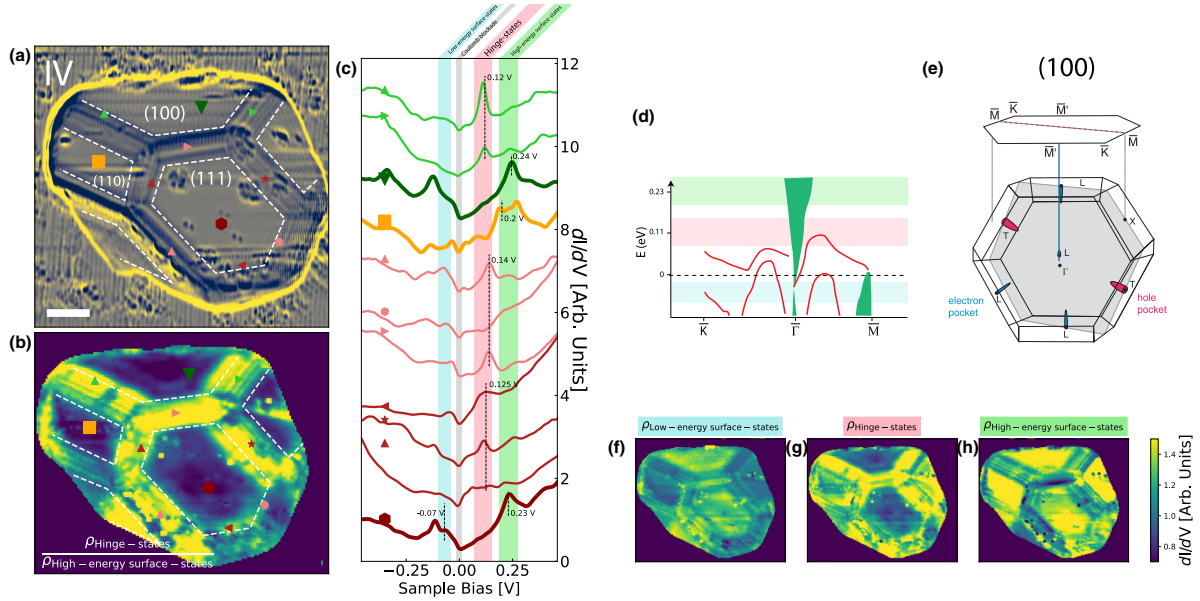
FIG. 3. STS data on nanocrystal IV. (a) Laplacian $\Delta_{xyz}z(x, y)$ transform of a topographic STM image ($I_{set} = 30$ pA, $V_{bias} = 1.5$ V). The scale bar is 5-nm long. (b) Conductance map $\frac{\rho_{HS}}{\rho_{HESS}}$ obtained by taking the ratio of the DC integrated on energy range of hinge-states ρ_{HS} with the DC integrated on energy range of high-energy surface-states ρ_{HESS}. The scale is the same as panel (a). (c) DC for selected points indicated as colored symbols on panels (a) and (b). The vertical colored rectangles indicate the energy ranges of interest corresponding, respectively, to low-energy surface states, Coulomb gap, hinge states, and high-energy surface states. The vertical dashed lines indicates conductance peaks of interest. See the text. (d) Extracted from Ref. [46], the relations dispersions of projected bulk states (green areas), surface states (red lines), and hinge states (blue line) on the (100) facet. (e) Bulk Brillouin zone and pseudo-Brillouin zone of the (100) facet. (f)–(h) Conductance maps ρ_{LESS}, ρ_{HS}, and ρ_{HESS} obtained by integrating the DCs on energy range of low-energy surface states, hinge states, and high-energy surface states, respectively.

spectral feature of interest in this energy range on the whole nanocrystal.

To obtain maps of the local density of states, we remove the effects of changing tip-height and tunnel barrier energy by normalizing the DC spectra assuming that the total density of states is conserved on the energy range [−0.5 to 0.5 eV] measured. That is, the DC $\frac{dI}{dV}(V)$ spectra are normalized by their integrated values $\int_{-0.5}^{0.5} \frac{dI}{dV} dV$. Then, the normalized spectra are integrated on the three energy ranges corresponding to high-energy surface states [0.19, 0.27 V], low-energy surface-states [−0.1, -0.04 V] and hinge states [0.07, 0.15 V], to give ρ_{HESS}, ρ_{LESS}, and ρ_{HS}, respectively, shown Figs. 2(i),–2(k), and 3(f)–3(h) for nanocrystal I and nanocrystal IV, respectively.

At the energy of high-energy surface states, Figs. 2(k) and 3(h), a large density of states is visible on all facets except on the edges. In contrast, at the energy of van Hove singularities due to hinge states, Figs. 2(j) and 3(g), a large density of states is observed on almost all hinges, between the (111) facet and (110), (100) facets as well as between the (110) facets and the (100) facets. Note that a large density of hinge states, is also observed in the middle of the largest (110) facet of nanocrystal I, surrounded by white continuous lines in Fig. 2(j), seemingly as a consequence of the defect observed in the topography, Fig. 2(a). Note also that the density of low-energy surface states is mostly visible on the (111) and (100) facets and not on the (110) facets. Looking at the conductance maps Figs. 2(j), 2(k), 3(g), and 3(h) for both nanocrystal I and nanocrystal IV, respectively, the anticorrelation between the

density of surface-states ρ_{HESS}, and the density of hinge states in the van Hove singularities ρ_{HS}, is obvious. This suggests that a map of hinge states can be obtained by calculating the ratio ρ_{HS}/ρ_{HESS}, which is shown Figs. 2(b) and 3(b) for both nanocrystal I and nanocrystal IV, respectively. In addition, Fig. 4 show the topography, ratio ρ_{HS}/ρ_{HESS} and DC spectra for the three additional nanocrystals: II, III, and V.

For all nanocrystals, the map ρ_{HS}/ρ_{HESS} shows that the topological states are clearly visible only at the hinges where two distinct Bi facets are well defined. See how the conductance peaks due to hinge states disappear where the (111) facet reaches the InAs surface. This suggests that the hinge states indeed arise from the interaction between surface states as expected theoretically. More precisely, the theoretical model proposed in Ref. [17] implies the existence of two sets of surface states resulting from two copies of the three-dimensional Z_2 topological insulator. The off-diagonal coupling between the two sets opens a gap for the surface states, leaving only in-gap hinge states at the edges of the facets. Thus, our STM/STS study of nanocrystals confirm the existence of hinge states and so the classification of Bi as a HOTI.

To this topological interpretation, one could oppose a more trivial interpretation where the hinge states result from chemical defects, such as dangling bonds, at the facet edges. However, this interpretation is not consistent with the observation of hinge states along the diagonals in the middle of (110) facets of nanocrystal I, Fig. 2(b), nanocrystal III, Fig. 4(e), and nanocrystal V, Fig. 4(h). For easy identification, they are surrounded by white continuous lines in those figure panels.
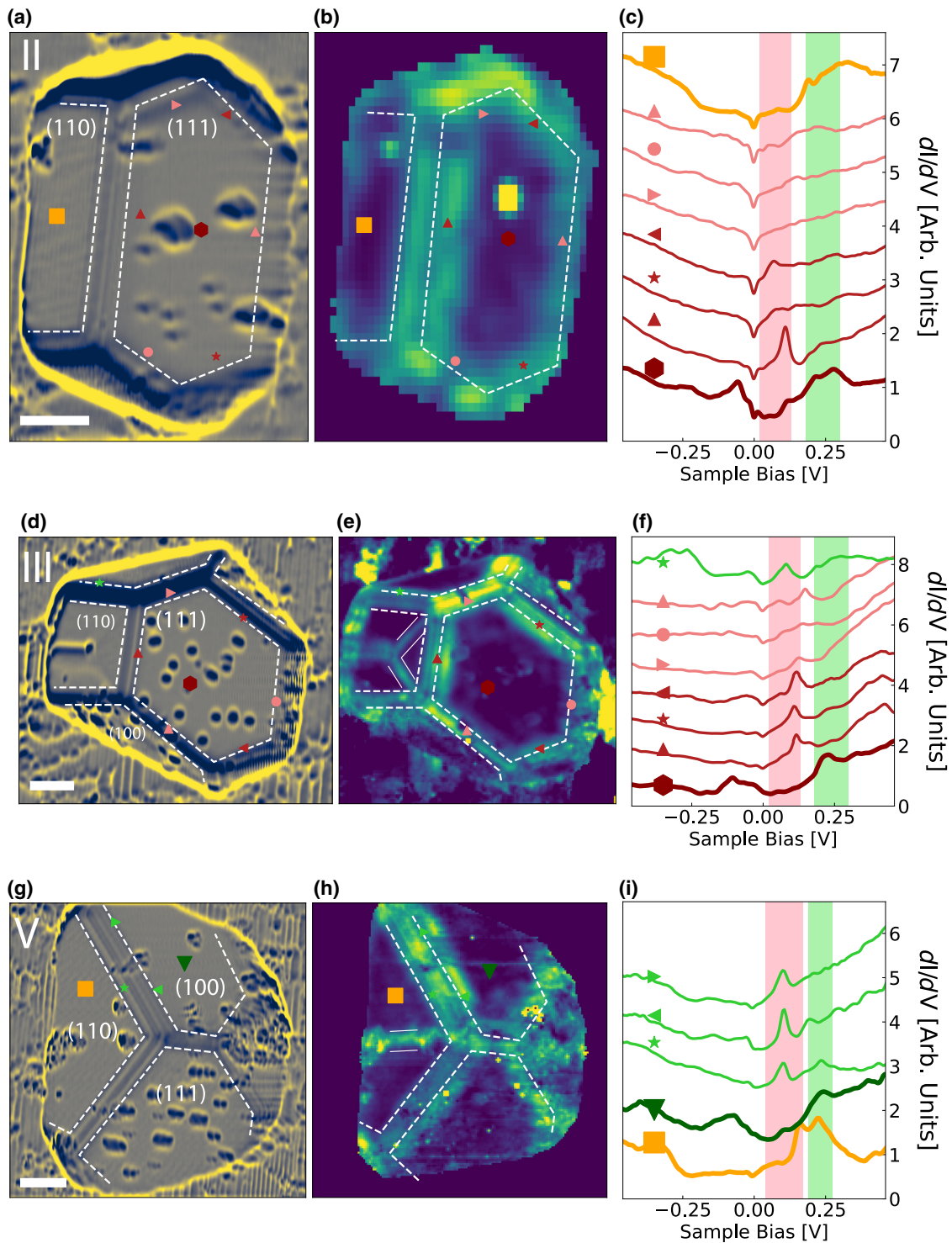
FIG. 4. (a)–(c) STM/STS data for nanocrystal II. (a) Laplacian $\Delta_{xy}z(x, y)$ transform of a topographic STM image ($I_{set} = 30$ pA, $V_{bias} =$ 1.5 V). The scale bar is 5-nm long. The dashed lines indicate the edges between facets. (b) Conductance map $\frac{\rho_{HS}}{\rho_{HESS}}$ obtained by taking the ratio of the DC integrated on energy range of hinge-states ρ_{HS} with the DC integrated on the energy range of high-energy surface-states ρ_{HESS}. The scale is the same as in panel (a). The dashed lines indicate the edges between facets. (c) DC for selected points indicated as colored symbols in panels (a) and (b). The vertical colored rectangles indicate the energy ranges of interest corresponding, respectively, to the hinge states and high-energy surface-states. (def) STM/STS data for nanocrystal III. (e) The continuous lines indicates the diagonal states generated by the defect in the middle of the (110) facet visible in panel (d). Note how they merge with the hinge states. (ghi) STM/STS data for nanocrystal V.
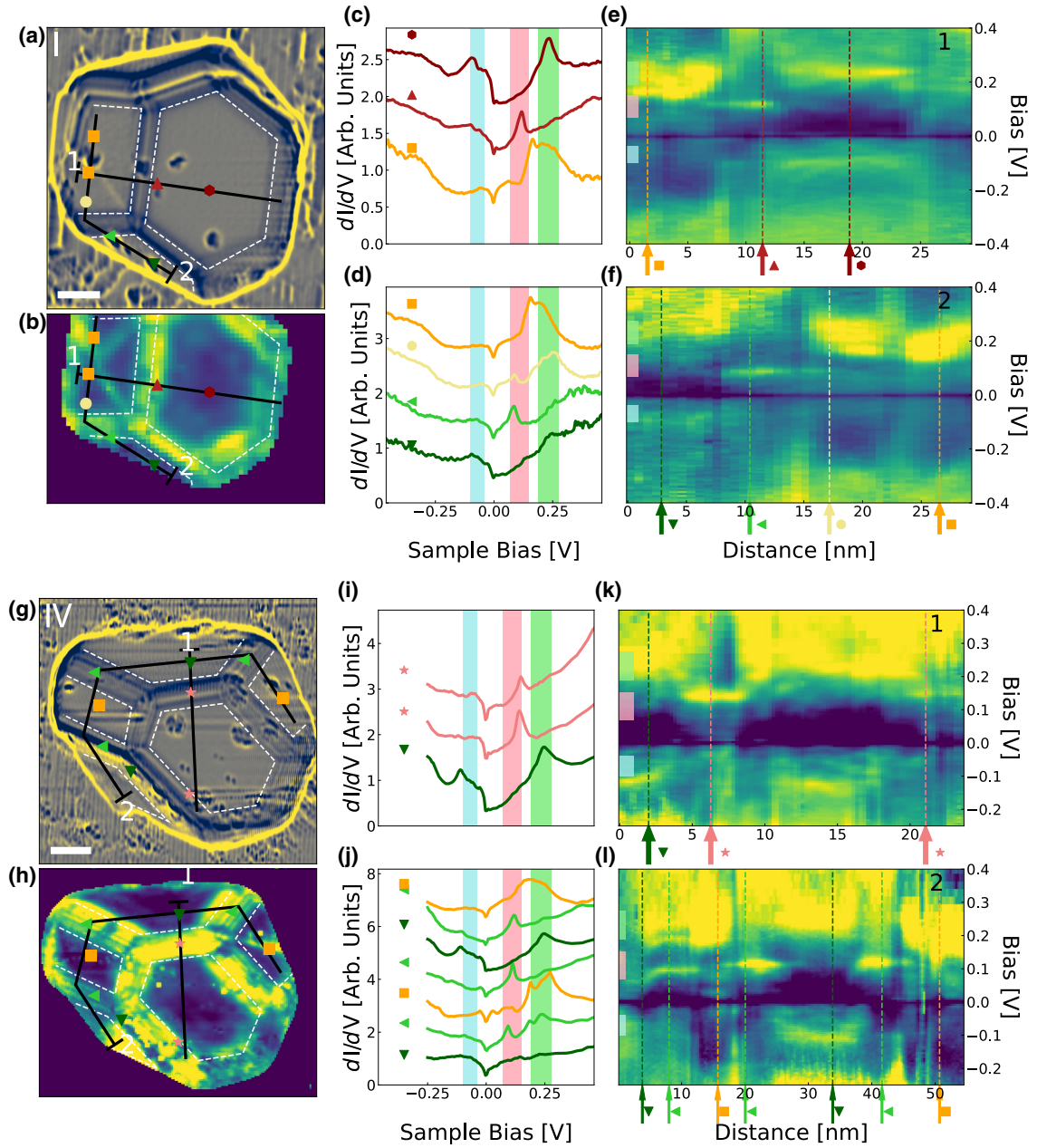
FIG. 5. STM/STS data for nanocrystal I. (a) Laplacian $\Delta_{xyz}z(x,y)$ transform of a topographic STM image ($I_{set} = 30$ pA, $V_{bias} = 1.5$ V). The scale bar is 5-nm long. (b) Conductance map $\frac{\rho_{HS}}{\rho_{HESS}}$ obtained by taking the ratio of the DC integrated on energy range of hinge-states ρ_{HS} with the DC integrated on energy range of high-energy surface-states ρ_{HESS}. The scale is the same as in panel (a). (c) and (d) DC for selected points indicated as colored symbols in panels (a) and (b) and indicated as vertical dashed lines in panels (e) and (f). (e) and (f) Conductance maps as a function of sample bias and distance along the profiles drawn as black lines in panels (a) and (b). (g)–(l) STM/STS data for nanocrystal IV.

Although these diagonal states seem to be the consequence from adatoms/defects in the middle of the (110) facet as visible on the corresponding topographies, they are remarkable as they exist all along the diagonal of the (110) facets even where no defect is present. Furthermore, they are clearly seen to merge with the hinge states on the edge with the (111) facet. This observation suggests that these diagonal states are not related to local chemical defects, instead, they are related to the hinge-states and are circling around the nanocrystal as expected for topological hinge states.

IV. DISCUSSION

Despite global consistency of the STS data with a HOTI model, there are two features that remain be understood theoretically. First, as mentioned above, the spectral weight associated with the hinge states in the van Hove singularities appears concomitantly with the disappearance of the spectral weight associated with the high-energy surface states. To highlight this anticorrelation between high-energy surface states and hinge states, Figures 5(e), 5(f), 5(k) and 5(l) show the DC maps as function of sample voltage and distance along
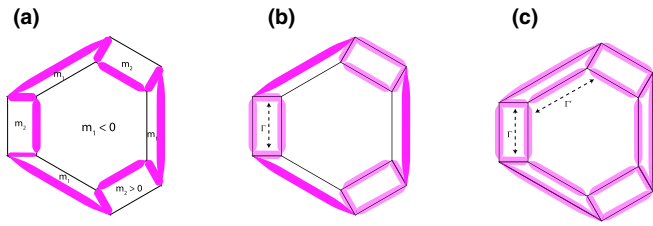
FIG. 6. Illustration of tunnel coupling between hinge states. (a) In the absence of tunnel-coupling between opposite edges, the hinge-states encircle the nanocrystal following hinges where the gap (mass) changes sign between two facets, as described in Ref. [17]. (bc) In presence of tunnel-coupling Γ or Γ', the hinge-states become distributed on all edges.

profiles drawn on the topographic images Figs. 5(a) and 5(g) and ratio maps Figs. 5(b) and 5(h) for nanocrystal I (IV). These maps show that the hinge states appear at the expense of the surface states on all facets. From the model of Ref. [17], we expect that the gap should remain constant on the whole surface of the nanocrystal, including the hinges; however, a redistribution of surface states at the approach of the hinge can be expected but has not been discussed theoretically.

Second, according to this model applied to a rod of hexagonal section [17], the hinge states should not exist on all hinges, but only on those separating facets with Dirac masses of opposite signs. Instead, we observe topological states on all hinges except where the facet reaches the InAs substrate. We suggest that this ubiquitous presence result from the coupling between hinge states on opposite sides of the facets. Indeed, it is well established that the tunnel coupling between the edge states at opposite edges (surfaces) of a two-dimensional (three-dimensional) topological insulator leads to hybridization between edge states and to a gap opening in the relation dispersion of the edge-states Dirac spectrum [23,27,51–53]. This is also true for second-order topological insulator as shown recently for the corner states of a two-dimensional second-order topological insulator [54]. In this last theoretical work, it has been shown that for well *localized* corner states, the corresponding density of states is large on only some of the corners and not on others, however, when the wave functions of corner states overlap, the corresponding density of states become equally distributed on all corners. As illustrated Fig. 6, in our small nanocrystals, significant overlaps of the wave functions describing the hinge states located at opposite edges is to be expected, this could explain their presence on all hinges as well as the slightly different energy position of

the van Hove singularities observed for different hinges due to gap opening in their relation dispersion. The possibility of a large coupling between hinge states located at different edges is substantiated by a recent *ab initio* study of bismuth [55] indicating a deep penetration of the surface states within the bulk and that bismuth should be considered bulklike only for thicknesses larger than 400 nm.

Although the effect of tunnel coupling between corner states has been analyzed from tight-binding calculations on a two-dimensional lattice [54], the heavy computational cost for three-dimensional nanocrystals prevented us to perform such a tight-binding calculation. Furthermore, at hinges where several atomic steps exists, individual hinge states separated in space by terraces should exist and for an even number of such states, they can hybridize and gap out. Note also that the observation of a van Hove singularity conductance peak does not imply that the hinge state is topological. It is possible that only some of the hinge states are gapless, whereas, others are gapped, however, on the background of all the conducting states such a gap is difficult to observe by STM.

V. CONCLUSION

To summarize, we have shown that Bi nanocrystals could be grown on the (110) InAs surface. Their size in the tens of nanometer make them suitable for STM/STS studies on all facets of the tridimensional nanocrystal. We identified the hinge states van Hove singularities at all hinges between the three facets (111), (110), and (100), however, on edges where the facet ends on the InAs substrate, no van Hove singularity is observed. These observations are consistent with the classification of Bi as a HOTI. We suggest that the ubiquitous observation of the van Hove singularities on all hinges result from their coupling across the nanometer-sized facets. Further theoretical and numerical simulations are needed to confirm this suggestion.

ACKNOWLEDGMENTS

[1] M. Tinkham, *Group Theory and Quantum Mechanics* (Dover, New York, 2003).

[2] J. Zak, Band representations of space groups, Phys. Rev. B **26**, 3010 (1982).

[3] J. Cano, B. Bradlyn, Z. Wang, L. Elcoro, M. G. Vergniory, C. Felser, M. I. Aroyo, and B. A. Bernevig, Building blocks of topological quantum chemistry: Elementary band representations, Phys. Rev. B **97**, 035139 (2018).

[4] B. Bradlyn, L. Elcoro, J. Cano, M. G. Vergniory, Z. Wang, C. Felser, M. I. Aroyo, and B. A. Bernevig, Topological quantum chemistry, Nature (London) **547**, 298 (2017).

[5] H. C. Po, A. Vishwanath, and H. Watanabe, Symmetry-based indicators of band topology in the 230 space groups, Nat. Commun. **8**, 50 (2017).

[6] Z. Song, T. Zhang, Z. Fang, and C. Fang, Quantitative mappings between symmetry and topology in solids, Nat. Commun. **9**, 3530 (2018).

[7] E. Khalaf, H. C. Po, A. Vishwanath, and H. Watanabe, Symmetry Indicators and Anomalous Surface States of Topological Crystalline Insulators, Phys. Rev. X **8**, 031070 (2018).

[8] B. J. Wieder, B. Bradlyn, J. Cano, Z. Wang, M. G. Vergniory, L. Elcoro, A. A. Soluyanov, C. Felser, T. Neupert, N. Regnault,

and B. A. Bernevig, Topological materials discovery from crystal symmetry, Nat. Rev. Mater. **7**, 196 (2021).

[9] M. Z. Hasan and C. L. Kane, Colloquium: Topological insulators, Rev. Mod. Phys. **82**, 3045 (2010).

[10] X.-L. Qi and S.-C. Zhang, Topological insulators and superconductors, Rev. Mod. Phys. **83**, 1057 (2011).

[11] J. C. Y. Teo, L. Fu, and C. L. Kane, Surface states and topological invariants in three-dimensional topological insulators: Application to Bi$_-$xSb$_x$, Phys. Rev. B **78**, 045426 (2008).

[12] L. Fu, Topological Crystalline Insulators, Phys. Rev. Lett. **106**, 106802 (2011).

[13] C. Fang and L. Fu, New classes of topological crystalline insulators having surface rotation anomaly, Sci. Adv. **5**, eaat2374 (2019).

[14] Z. Song, Z. Fang, and C. Fang, (d-2)-dimensional edge states of rotation symmetry protected topological states, Phys. Rev. Lett. **119**, 246402 (2017).

[15] F. Schindler, A. M. Cook, M. G. Vergniory, Z. Wang, S. S. P. Parkin, B. Andrei Bernevig, and T. Neupert, Higher-order topological insulators, Sci. Adv. **4**, eaat0346 (2018).

[16] E. Khalaf, Higher-order topological insulators and superconductors protected by inversion symmetry, Phys. Rev. B **97**, 205136 (2018).

[17] F. Schindler, Z. Wang, M. G. Vergniory, A. M. Cook, A. Murani, S. Sengupta, A. Y. Kasumov, R. Deblock, S. Jeon, I. Drozdov, H. Bouchiat, S. Guéron, A. Yazdani, B. A. Bernevig, and T. Neupert, Higher-Order topology in bismuth, Nat. Phys. **14**, 918 (2018).

[18] Z. Wang, B. J. Wieder, J. Li, B. Yan, and B. A. Bernevig, Higher-Order topology, monopole nodal lines, and the origin of large fermi arcs in transition metal dichalcogenides XTe$_2$ (X = Mo,W), Phys. Rev. Lett. **123**, 186401 (2019).

[19] D. Hsieh, D. Qian, L. Wray, Y. Xia, Y. S. Hor, R. J. Cava, and M. Z. Hasan, A topological dirac insulator in a quantum spin hall phase, Nature (London) **452**, 970 (2008).

[20] B. J. Wieder, B. Bradlyn, Z. Wang, J. Cano, Y. Kim, H.-S. D. Kim, A. M. Rappe, C. L. Kane, and B. A. Bernevig, Wallpaper fermions and the nonsymmorphic dirac insulator, Science **361**, 246 (2018).

[21] I. K. Drozdov, A. Alexandradinata, S. Jeon, S. Nadj-Perge, H. Ji, R. J. Cava, B. Bernevig, and A. Yazdani, One-dimensional topological edge states of bismuth bilayers, Nat. Phys. **10**, 664 (2014).

[22] S. Murakami, Quantum Spin Hall Effect and Enhanced Magnetic Response by Spin-Orbit Coupling, Phys. Rev. Lett. **97**, 236805 (2006).

[23] M. Wada, S. Murakami, F. Freimuth, and G. Bihlmayer, Localized edge states in two-dimensional topological insulators: Ultrathin Bi films, Phys. Rev. B **83**, 121310 (2011).

[24] L. Peng, J.-J. Xian, P. Tang, A. Rubio, S.-C. Zhang, W. Zhang, and Y.-S. Fu, Visualizing topological edge states of single and double bilayer Bi supported on multibilayer Bi(111) films, Phys. Rev. B **98**, 245108 (2018).

[25] F. Yang, J. Jandke, T. Storbeck, T. Balashov, A. Aishwarya, and W. Wulfhekel, Edge states in mesoscopic bi islands on superconducting nb(110), Phys. Rev. B **96**, 235413 (2017).

[26] F. Reis, G. Li, L. Dudy, M. Bauernfeind, S. Glass, W. Hanke, R. Thomale, J. Schäfer, and R. Claessen, Bismuthene on a SiC substrate: A candidate for a high-temperature quantum spin hall material, Science **357**, 287 (2017).

[27] R. Stühler, A. Kowalewski, F. Reis, D. Jungblut, F. Dominguez, B. Scharf, G. Li, J. Schäfer, E. M. Hankiewicz, and R. Claessen, Effective lifting of the topological protection of quantum spin hall edge states by edge coupling, Nat. Commun. **13**, 3480 (2022).

[28] S. Salehitaleghani, T. Maerkl, P. J. Kowalczyk, M. Le Ster, X. Wang, G. Bian, T.-C. Chiang, and S. A. Brown, Edge states of α-bismuthene nanostructures, 2D Mater. **10**, 015020 (2022).

[29] B. Rasche, A. Isaeva, M. Ruck, S. Borisenko, V. Zabolotnyy, B. Büchner, K. Koepernik, C. Ortix, M. Richter, and J. van den Brink, Stacked topological insulator built from bismuth-based graphene sheet analogues, Nature Mater. **12**, 422 (2013).

[30] C. Pauly, B. Rasche, K. Koepernik, M. Liebmann, M. Pratzer, M. Richter, J. Kellner, M. Eschbach, B. Kaufmann, L. Plucinski, C. M. Schneider, M. Ruck, J. van den Brink, and M. Morgenstern, Subnanometre-wide electron channels protected by topology, Nat. Phys. **11**, 338 (2015).

[31] A. Marrazzo, M. Gibertini, D. Campi, N. Mounet, and N. Marzari, Prediction of a Large-Gap and Switchable Kane-Mele Quantum Spin Hall Insulator, Phys. Rev. Lett. **120**, 117701 (2018).

[32] J. I. Facio, S. K. Das, Y. Zhang, K. Koepernik, J. van den Brink, and I. C. Fulga, Dual topology in jacutingaite Pt$_2$HgSe$_3$, Phys. Rev. Mater. **3**, 074202 (2019).

[33] A. Marrazzo, N. Marzari, and M. Gibertini, Emergent dual topology in the three-dimensional Kane-Mele Pt$_2$HgSe$_3$, Phys. Rev. Res. **2**, 012063(R) (2020).

[34] I. Cucchi, A. Marrazzo, E. Cappelli, S. Riccò, F. Y. Bruno, S. Lisi, M. Hoesch, T. K. Kim, C. Cacho, C. Besnard, E. Giannini, N. Marzari, M. Gibertini, F. Baumberger, and A. Tamai, Bulk and surface electronic structure of the Dual-Topology semimetal Pt$_2$HgSe$_3$, Phys. Rev. Lett. **124**, 106402 (2020).

[35] R. Noguchi, M. Kobayashi, Z. Jiang, K. Kuroda, T. Takahashi, Z. Xu, D. Lee, M. Hirayama, M. Ochi, T. Shirasawa, P. Zhang, C. Lin, C. Bareille, S. Sakuragi, H. Tanaka, S. Kunisada, K. Kurokawa, K. Yaji, A. Harasawa, V. Kandyba, et al., Evidence for a higher-order topological insulator in a three-dimensional material built from van der waals stacking of bismuth-halide chains, Nature Mater. **20**, 473 (2021).

[36] A. Bernard, Y. Peng, A. Kasumov, R. Deblock, M. Ferrier, F. Fortuna, V. T. Volkov, Y. A. Kasumov, Y. Oreg, F. von Oppen, H. Bouchiat, and S. Guéron, Long-lived andreev states as evidence for protected hinge modes in a bismuth nanoring josephson junction, Nat. Phys. **19**, 358 (2023).

[37] Y.-B. Choi, Y. Xie, C.-Z. Chen, J. Park, S.-B. Song, J. Yoon, B. J. Kim, T. Taniguchi, K. Watanabe, J. Kim, K. C. Fong, M. N. Ali, K. T. Law, and G.-H. Lee, Evidence of higher-order topology in multilayer WTe$_2$ from josephson coupling through anisotropic hinge states, Nature Mater. **19**, 974 (2020).

[38] A. Kononov, G. Abulizi, K. Qu, J. Yan, D. Mandrus, K. Watanabe, T. Taniguchi, and C. Schönenberger, One-Dimensional edge transport in Few-Layer WTe$_2$, Nano Lett. **20**, 4228 (2020).

[39] C. Huang, A. Narayan, E. Zhang, X. Xie, L. Ai, S. Liu, C. Yi, Y. Shi, S. Sanvito, and F. Xiu, Edge superconductivity in multilayer WTe$_2$ josephson junction, Natl. Sci. Rev. **7**, 1468 (2020).

[40] C.-H. Hsu, X. Zhou, T.-R. Chang, Q. Ma, N. Gedik, A. Bansil, S.-Y. Xu, H. Lin, and L. Fu, Topology on a new facet of bismuth, Proc. Natl. Acad. Sci. USA **116**, 13255 (2019).

[41] L. Aggarwal, P. Zhu, T. L. Hughes, and V. Madhavan, Evidence for higher order topology in Bi and Bi0.92Sb0.08, Nat. Commun. **12**, 4420 (2021).

[42] S. Vlaic, S. Pons, T. Zhang, A. Assouline, A. Zimmers, C. David, G. Rodary, J.-C. Girard, D. Roditchev, and H. Aubin, Superconducting parity effect across the anderson limit, Nat. Commun. **8**, 14549 (2017).

[43] T. Zhang, S. Vlaic, S. Pons, A. Assouline, A. Zimmers, D. Roditchev, H. Aubin, G. Allan, C. Delerue, C. David, G. Rodary, and J.-C. Girard, Quantum confinement effects in pb nanocrystals grown on InAs, Phys. Rev. B **97**, 214514 (2018).

[44] W. G. Schmidt, Adsorption of group-v elements on III–V (1 1 0) surfaces, Surf. Sci. Rep. **25**, 141 (1996).

[45] M. G. Betti, D. Berselli, C. Mariani, N. Jedrecy, M. Sauvage-Simkin, Y. Garreau, and R. Pinchaux, (1×2) bi chain reconstruction on the InAs(110) surface, Phys. Rev. B **59**, 15760 (1999).

[46] P. Hofmann, The surfaces of bismuth: Structural and electronic properties, Prog. Surf. Sci. **81**, 191 (2006).

[47] Y. M. Koroteev, G. Bihlmayer, J. E. Gayone, E. V. Chulkov, S. Blügel, P. M. Echenique, and P. Hofmann, Strong Spin-Orbit Splitting on Bi Surfaces, Phys. Rev. Lett. **93**, 046403 (2004).

[48] Y. M. Koroteev, G. Bihlmayer, E. V. Chulkov, and S. Blügel, First-principles investigation of structural and electronic properties of ultrathin bi films, Phys. Rev. B **77**, 045428 (2008).

[49] A. Takayama, T. Sato, S. Souma, and T. Takahashi, Rashba effect in antimony and bismuth studied by spin-resolved ARPES, New J. Phys. **16**, 055004 (2014).

[50] A. Takayama, T. Sato, S. Souma, T. Oguchi, and T. Takahashi, One-Dimensional Edge States with Giant Spin Splitting in a Bismuth Thin Film, Phys. Rev. Lett. **114**, 066402 (2015).

[51] B. Zhou, H.-Z. Lu, R.-L. Chu, S.-Q. Shen, and Q. Niu, Finite Size Effects on Helical Edge States in a Quantum Spin-Hall System, Phys. Rev. Lett. **101**, 246807 (2008).

[52] Y. Zhang, K. He, C.-Z. Chang, C.-L. Song, L.-L. Wang, X. Chen, J.-F. Jia, Z. Fang, X. Dai, W.-Y. Shan, S.-Q. Shen, Q. Niu, X.-L. Qi, S.-C. Zhang, X.-C. Ma, and Q.-K. Xue, Crossover of the three-dimensional topological insulator Bi_2Se_3 to the two-dimensional limit, Nat. Phys. **6**, 584 (2010).

[53] J. Jung, A. Odobesko, R. Boshuis, A. Szczerbakow, T. Story, and M. Bode, Systematic Investigation of the Coupling between One-Dimensional Edge States of a Topological Crystalline Insulator, Phys. Rev. Lett. **126**, 236402 (2021).

[54] N. Arai and S. Murakami, Anisotropic penetration depths of corner states in a Higher-Order topological insulator, J. Phys. Soc. Jpn. **90**, 074711 (2021).

[55] I. Aguilera, H.-J. Kim, C. Friedrich, G. Bihlmayer, and S. Blügel, Z_2 topology of bismuth, Phys. Rev. Mater. **5**, L091201 (2021).